A semi-analytical thermal modelling approach for selective laser melting

Yang, Y.; Knol, Marius; van Keulen, F.; Ayas, C.

DOI
10.1016/j.addma.2018.03.002

Publication date
2018

Document Version
Accepted author manuscript

Published in
Additive Manufacturing

Link to formal publication "Additive Manufacturing" (Elsevier): https://doi.org/10.1016/j.addma.2018.03.002

A semi-analytical thermal modelling approach for selective laser melting

Y.Yang[a], M.F. Knol[a], F. van Keulen[a], C. Ayas[a,*]

[a]*Structural Optimization and Mechanics Group, Department of Precision and Microsystems Engineering, Faculty of Mechanical, Maritime and Material Engineering, Delft University of Technology, Mekelweg 2, 2628 CD, Delft, The Netherlands*

Abstract

Selective laser melting (SLM) wherein a metal part is built in a layer-by-layer manner in a powder bed is a promising and versatile way for manufacturing components with complex geometry. However, components built by SLM suffer from substantial deformation of the part and residual stresses. Residual stresses arise due to temperature gradients inherent to the process and the accompanying deformation. It is well known that the SLM process parameters and the laser scanning strategy have a substantial effect on the temperature transients of the part and henceforth on the degree of deformations and residual stresses. In order to provide a tool to investigate this relation, a semi-analytical thermal model of the SLM process is presented which determines the temperature evolution in a 3D part by way of representing the moving laser spot with a finite number of point heat sources. The solution of the thermal problem is constructed from the superposition of analytical solutions for point sources which are known in semi-infinite space and complimentary numerical/analytical fields to impose the boundary conditions. The unique property of the formulation is that numerical discretisation of the problem domain is decoupled from the steep gradients in the temperature field associated with localised laser heat input. This enables accurate and numerically tractable simulation of the process. The predictions of this semi-analytical model are validated by experiments and the exact solution known for a simple thermal problem. Simulations for building a complete layer using two different scanning patterns and subsequently building of multiple layers with constant and rotating scanning patterns in successive layers are performed. The computational efficiency of the semi-analytical tool is assessed which demonstrates its potential to gain physical insight in the full SLM process with acceptable computational costs.

Keywords: Additive manufacturing, SLM, cost efficient thermal modelling, scanning strategy, semi-analytical model, Superposition principle

1. Introduction

Additive manufacturing (AM) also known as '3D printing' is the generic name for building three dimensional objects by way of laying down successive thin slices of the object in a layer-by-layer manner [1]. This is contrary to conventional manufacturing techniques involving multiple steps where the final shape of the component is achieved, for instance, by casting, forming, and material removal. AM processes are rapidly advancing and thus enable fabrication of complex components with high topological freedom within a single manufacturing step. The unique advantage of AM is that, as the geometrical complexity of the object increases, no additional process time or cost get introduced [1].

Selective laser melting (SLM) is a Powder Bed Fusion (PBF) process as per ISO/ASTM 52900 and is the most common AM technique suitable for producing metal parts. In SLM, the build process of the product starts on a metal base plate placed inside an inert atmosphere as illustrated in Fig. 1. A thin layer of powder, typically having a thickness of 20 – 100 μm [2, 3], is spread with a recoater blade across the build area. Next, a focussed laser beam, having an energy sufficient to locally melt the metal powder, is directed onto the powder bed with a scanning mirror. The laser beam is scanned over the powder bed in such a way that it selectively melts and fuses powder particles to form the cross-sectional slice of the product upon solidification. The surrounding powder which has not been irradiated with the laser beam remains loose and serves as a support for the subsequent powder layers. Next, the build platform is lowered for a distance equal to the powder layer thickness and a new layer of powder is laid and levelled with the recoater blade. The laser beam scans the subsequent slice. While the laser scanning is applied, in addition to the powder layer, the previous solid layer is also partially locally melted so that during subsequent solidification, a seamless connection across the layers is achieved [4]. The process is repeated until the complete three dimensional object is built, typically consisting of hundreds of layers. If any of the layers is unable to sufficiently support the next one, support structures may be required to eliminate overhanging. Support structures also prevent overheating and restrict deformations. However, they increase the build time and material cost. Finally, the object is cut from the base plate and support structures are removed, loose powder is cleaned off and optionally a final finishing process is performed [3].

SLM can produce parts with densities up to 99.9% of the theoretical density [5] (i.e., with virtually no porosity) and mechanical properties similar to those produced by conventional

*Corresponding author
Email address: C.Ayas@tudelft.nl (C. Ayas)

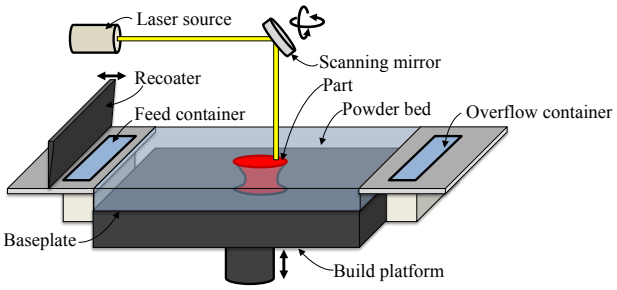

Figure 1: Schematic illustration of the building of a part submerged into a powder bed and fixed on the build platform. The laser source is directed by the scanning mirror in order to melt the uppermost layer of powder. Once the laser scanning of the current layer is finished, the recoater lays the next layer of powder from the feed container. Excess powder is stored in the overflow container.

manufacturing techniques [5, 6]. Although SLM parts exhibit a surface waviness, critical for cyclic loading, high surface quality can often be achieved with a finishing process [7, 8]. Moreover, since SLM provides an unprecedented form freedom, design tools such as topology optimisation can be fully exploited [9]. However, a major issue in the SLM process is the distortion of the part due to deformations induced during manufacturing and residual stresses associated with the deformations that are constrained. Deformations and residual stresses induced during SLM originate from thermal expansion/contraction cycles, shrinkage due to solidification and other volume changes due to solid state phase transformations. Severe deformations may disqualify the product for use and can cause jamming of the recoater, while residual stresses may cause failure, if a critical level is exceeded during the build [10, 11]. Residual stresses can also shorten the service life and give rise to degradation of the mechanical performance. However, generally a stress relief heat treatment is applied subsequent to the build in order to eliminate residual stresses in the final product.

SLM process parameters such as laser power, laser scanning velocity and pattern have been shown to influence both the amount of porosity and the deformations and the associated residual stresses [12, 13]. Therefore it is of paramount importance to determine the optimal set of process parameters for which the deformations, residual stresses and porosity are minimal for a given part geometry. Currently, the process parameters are being tuned empirically by way of trial-and-error, i.e., a test part is printed using different process parameters and those leading to the best quality are adopted [14, 15]. This is a time consuming and costly process requiring many printing jobs. Numerous iterations are usually needed before a satisfactory performance is obtained for mechanically demanding or high precision components. Moreover, the procedure needs to be repeated for different materials and part geometries.

Alternatively, SLM process models, capturing the essential physics of the process can be used to predict the resulting porosity, deformation and residual stress for a given set of process parameters. Therefore SLM process models can be instrumental to determine the optimal process parameters. Ideally, the process model needs to be both accurate and computationally tractable in order to fully replace the empirical approach outlined above. However, the SLM process involves the coupling of a number of physical phenomena such as heat transfer, fluid dynamics, phase transformations and solid mechanics [16]. Therefore, it is a complicated multi-physics problem to analyse which also requires a due account for the geometry of the part to be built. Moreover, the transient nature of the heat transfer phenomena and the presence of steep temperature gradients in the vicinity of the laser spot further complicate the problem from a numerical point of view. Recall that thermal expansion/contraction cycles are key for the part distortion and residual stress field [17, 18] and, thus, it is critical to determine the temperature transients as accurately as possible. The steep temperature gradients are present due to the local nature of heating in SLM. The laser beam has a spot radius typically on the order of tens of micrometers [19], while parts produced have dimensions typically on the order of tens of millimetres. This mismatch of characteristic length scales becomes prohibitive when a numerical scheme such as finite elements is used to solve the governing heat equation. This would require fine spatial and temporal discretisation to resolve the steep temperature gradients which in turn requires an excessive number of elements and time steps, resulting in very high computational costs.

So far, only a few studies have attempted to model the complete parts typically built with SLM. In these so called *global models* the total computational costs are reduced to allow for complete part modelling. For example, Papadakis *et al.* [20] and Zaeh and Branner [11] proposed a simplified representation of the heat input during the process. Instead of modelling a moving heat source, a heat input acting simultaneously on the whole object and homogeneous across the layer that is being built is assumed. Consequently, information concerning the scanning pattern is inherently lost. In contrast, the majority of the studies in literature investigate only a small fraction of the build-process, which will be subsequently referred to as *local models*. The local models are detailed, and may include description of the different phase transformations and small-scale phenomena such as convective heat flow inside the melt-pool. Moreover, due account for temperature dependent material properties can be made. However, a complete build analysis of a component or an extensive parametric study with local models is currently computationally intractable. Therefore, although the local models can provide deep insight of the SLM process, their use is restricted to very small spatial domains and they are not suitable for design purposes. For instance, Zeng *et al.* [21] reported a total computation time of 3763 hours for the addition of a single layer on a base plate of dimensions 42 mm $\times$7 mm $\times$ 3 mm. Although global models remain to be the pragmatic alternative, experiments in literature show that a strong correlation exists between the scanning pattern and the resulting residual stresses [22, 23, 24]. For example, Kruth *et al.* [22] measured the curling angle of a structure built with various scanning patterns and reported the bending can be reduced by a maximum of 59% with changing the scanning pattern only. This implies that any modelling effort in pursue of optimum SLM process parameters should explicitly take into account the

scanning pattern and be able to capture the effect of a given scanning pattern on the temperature evolution. Mohanty and Hattel [25, 26, 27, 28] developed a fast low fidelity model and studied the temperature evolution of a single layer with various scanning strategies. Upon comparing their predictions with a FE analysis having a mesh size sufficiently small to capture characteristic gradients of the temperature field, the low-fidelity model was able to reproduce average and maximum temperatures of the domain. However, the temperature field predictions of the low fidelity model was found to be different than that of the high fidelity FE model in the vicinity of the laser beam [26].

In this paper, we aim to develop a thermal process model of SLM also utilising the superposition principle suitable for a complete build analysis. Our formulation also accounts for the moving laser beam and hence captures the effects of different scanning patterns alongside other process parameters. Here, we exclusively focus on the thermal history of the part during the SLM process, since an accurate representation of the temperature distribution is a key intermediate step for an accurate prediction of deformations and residual stresses arising due to thermal strains encountered. For that purpose, we propose a semi-analytical modelling approach where the moving laser beam is represented with a set of point heat sources. The closed form analytical solution known for a point heat source is utilised to capture the steep temperature gradients in the vicinity of the laser beam in a transient manner. However, the analytical solution for a point heat source is only known for a few simple cases such as in a semi-infinite medium. Therefore boundary conditions of the problem at hand are enforced with image sources and a complementary correction field, solved numerically. The key advantage of our method is the ability to capture high temperature gradients in the vicinity of the laser spot, independent from the spatial discretisation applied for the complementary correction field. Consequently, a complete build analysis with high accuracy becomes computationally tractable with a relatively coarse spatial discretisation. We will demonstrate that the computational cost are sufficiently small which is promising to incorporate this model within topology optimisation for the design of SLM products. Generalised finite element (FE) schemes with suitable enrichment on a coarse mesh have been shown to capture steady state solutions for thermal problems exhibiting localised sharp thermal gradients [29]. However, for the transient heat problems of interest, required temporal resolution can still be computationally prohibitive for a fully numerical approach and thus we propose the semi-analytical approach where the analytical solution of point heat sources plays a crucial role. It is worth noting that utilising analytical solutions for Gaussian heat sources [26], Goldak sources [30] and moving point sources [30] have been investigated in the context of AM process modelling. However, in our approach the use of the superposition principle enables us to represent not only heat input due to laser scanning vectors but also to impose correct boundary conditions. The latter has not yet been reported in literature to the best of our knowledge and cannot be addressed with the use of analytical solutions only. It is the superposition of analytical and numerical correction fields that bridges the characteristic length scales of the laser spot and the part being built for the inherently multi-scale problem at hand.

The outline of the paper is as follows. Section 2 details the proposed semi-analytical model for temperature evolution during the SLM process. In Section 3, the accuracy of the semi-analytical model is validated by comparing its predictions with corresponding experimental and exact solutions available in literature. In Section 4, the semi-analytical model is used to simulate the SLM process of building a single layer and multiple layers, respectively. Different scanning patterns are considered to investigate their influence on the thermal history of the printed part and melt pool dimensions. The article concludes with a reiteration of the most salient points of the study.

2. Model description

Consider the SLM process of a three-dimensional body with an arbitrary shape. At time $t = 0$ the body V with a surface ∂V has already been built as sketched in Fig. 2a. The surface ∂V comprises of the top surface ∂V_{top}, the lateral surface ∂V_{lat} and the bottom surface ∂V_{bot}, i.e., $\partial V = \partial V_{\text{bot}} \cup \partial V_{\text{lat}} \cup \partial V_{\text{top}}$. At time $t = 0$, the body V is submerged into the powder bed as shown in Fig. 2b, where a thin layer of powder is also laid on top of the body. The top surface ∂V_{top} and the lateral surface ∂V_{lat} are hence covered with powder, while ∂V_{bot} is bonded to the base plate, see Fig 1. The origin of the coordinate system is located such that ∂V_{bot} corresponds to the x_1-x_2 plane and a right handed orthonormal basis is selected as shown in Fig. 2b. At time $t = 0$ the scanning of the laser starts over the uppermost powder layer with a predefined scanning pattern and the temperature of the body will increase as dictated by the heat equation

$$\rho c_p \frac{\partial T}{\partial t} = \nabla \cdot (k \nabla T) + Q, \qquad \text{in} \quad V, \tag{1a}$$

where T is the temperature, Q is the rate of volumetric heat generation, i.e. the source term, ρ, c_p and k are the density, the constant-pressure specific heat and the thermal conductivity, respectively. In order to determine the temperature development within the body V, we proceed to describe a boundary value problem (BVP) with relevant boundary conditions on ∂V and an initial condition $T(x_i, 0)$ at $t = 0$. We first observe that the mean conductivity[1] of the powder covering ∂V_{lat} and ∂V_{top} is approximately $1/100$ of that of the solid [19], hence it is justified to assume that powder has negligible conductivity and therefore the heat transfer between the solid and the powder is assumed to be negligible in our model. Next, we note that powder at ∂V_{top} is locally melted by the laser, enabling possible radiation and convection of heat. However, the amount of heat lost due to radiation and convection is also negligible in comparison to the amount of heat transferred by conduction within the solid body [32, 33] and, thus, radiation and convection effects are not included in our formulation. Consequently, a zero heat flux

[1] Upon treating the powder as a continuous media, a mean conductivity can be defined [31]

boundary condition is prescribed at ∂V_{lat} and ∂V_{top} as

$$\frac{\partial T}{\partial x_i} n_i = 0 \qquad \text{on} \quad \partial V_{\text{lat}}, \tag{1b}$$

$$\frac{\partial T}{\partial x_i} m_i = 0 \qquad \text{on} \quad \partial V_{\text{top}}, \tag{1c}$$

where n_i and m_i are the components of outward facing normal to ∂V_{lat} and ∂V_{top}, respectively and the repeated index implies summation over i. During the SLM process the base plate is typically pre-heated, and stays at this constant temperature [34, 35]. We take this into account by prescribing a temperature boundary condition on the bottom surface ∂V_{bot} that is bonded to the base plate as

$$T = T_c \qquad \text{on} \quad \partial V_{\text{bot}}, \tag{1d}$$

where T_c is the known base plate temperature.

It should be noted that during the SLM process, melting, solidification and solid state phase transformations take place within the body V. The solution of the BVP will be complicated by these phase transformations. In reality, the existence of latent heat will result in no temperature change during melting and only after complete melting is accomplished, the temperature will be rising. However, as the laser moves away from the material point of interest, the temperature will drop and solidification will occur. Now the same amount of latent heat will be emitted and thus temperature would be again constant for a brief period of time. Since melting and concurrent solidification phenomena occurring in body V are local and rapid so that it can be argued that the latent heat initially absorbed during melting is subsequently released during solidification within a short duration. Consequently, the net effect of these phase transformations on the total energy balance is zero and the influence of neglecting the latent heat in melting/solidification cycles is expected to be small. This assumption is also used for example in [36]. The energy for solid phase transformations is only a second-order effect when compared to the latent heat of melting/solidification [37] and henceforth is also neglected.

Next, consider the laser beam with a power P and a spot radius r scanning over the powder bed with a fixed speed of v. At time $t = 0$, the laser beam is irradiating at a known initial position on the powder bed. A small fraction of the incident laser beam is reflected while the rest is absorbed by the powder. The fraction of the energy absorbed is denoted by A and its value is approximated using the model proposed by Gusarov *et al.* [19].

The absorbed energy melts the powder locally, creating a melt-pool in the vicinity of the laser spot. Now recall that the conductivity of the powder surrounding a melt-pool is much less than that of the solid body and the heat loss from the free surface due to convection and radiation is also negligible [32, 33]. Therefore, the energy present in the melt-pool is by enlarge transmitted to the body V. This implies that the absorbed laser energy is essentially subjected directly to the body V via the surface ∂V_{top} which is immediately beneath the uppermost layer of powder. Consequently, in our model we discard the uppermost layer of powder and instead consider heat

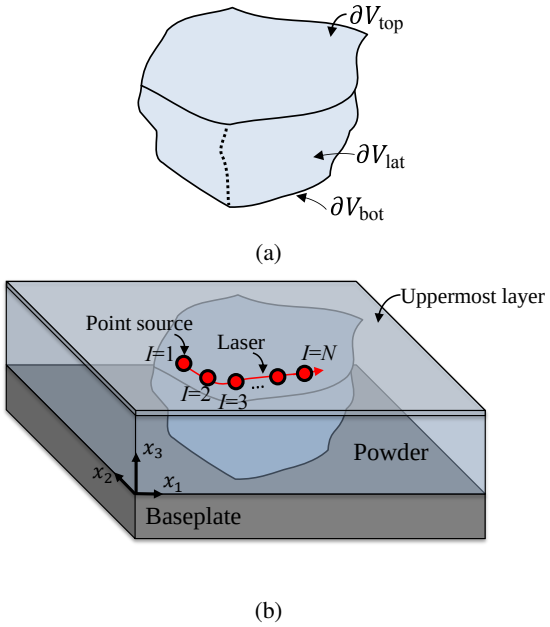

Figure 2: Schematic illustration of (a) the body V with its surface ∂V decomposed into ∂V_{top}, ∂V_{lat} and ∂V_{bot} and (b) body V submerged into the powder bed where it is bonded to the base plate at ∂V_{bot} and laser scanning is applied on the uppermost layer of powder.

sources at ∂V_{top} to represent the scanning of the laser. Although this assumption is reminiscent of the laser welding process, the thermal equations can be solved without updating the geometry. Hence, the computational efficiency can be enhanced significantly. The results in Section 3 will show that good accuracy can still be achieved.

2.1. A superposition method for the thermal problem

Even with above described simplifications, the solution of this BVP is numerically intractable due to the mismatch of length scales present in the problem. The laser spot radius r is typically 10–50 μm, while the characteristic length scale of the body is on the order of 10–100 mm. FE analysis of the BVP would require a local mesh size on the order of tens of microns to track the moving laser source. We therefore introduce another approximation to solve this problem.

First, we neglect the temperature dependence of the thermal parameters ρ, c_p and k in Eq. (1a), resulting in

$$\frac{\partial T}{\partial t} = \alpha \nabla^2 T + \frac{Q}{\rho c_p} \qquad \text{in} \quad V, \tag{2}$$

which is the linear heat equation and $\alpha = k/\rho c_p$ is the thermal diffusivity. It has been reported by Childs *et al.* [36] that, upon choosing suitable thermal parameters, the linear heat equation Eq. (2) is able to well approximate Eq. (1a).

Next, the laser scanning vector is discretised by a finite number of point heat sources, as shown in Fig. 2b. Point source I, where $I = 1, \ldots N$, is created at time $t_0^{(I)}$, while the next source $I + 1$ is created at time $t_0^{(I+1)} = t_0^{(I)} + \Delta t$ and Δt is the temporal step size for time integration. The location of each point

source is determined by the scanning pattern and neighbouring point sources are separated by $v\Delta t$. It remains to solve the BVP described by Eq. (1a) to determine the temperature distribution within the body V as a function of time while accounting for the point heat sources.

The solution of the linearised heat equation (2), is still complicated by the presence of the source term Q. However since Eq. (2) is linear, we can make use of the superposition principle in a manner similar to the method proposed by Ayas *et al.* [38]. The detailed formulation given below will show that the proposed solution strategy for Eq. (2) relies on an analytical solution which captures the high spatial gradients, complemented with a numerical solution which ensures compliance with boundary conditions. We therefore refer to this formulation in short as semi-analytical model.

Consider the body sketched in Fig. 3 where N point heat sources are created at ∂V_{top} to model a given laser scanning vector. The temperature field T is then decomposed as

$$T = \tilde{T} + \hat{T}, \tag{3}$$

where $\tilde{T}$ is the temperature field due to N point heat sources, each of which is created at a different time instant in accordance with the scanning history. The temperature field $\tilde{T}$ is expressed as

$$\tilde{T}(x_i, t) = \sum_{I=1}^{M} \tilde{T}^{(I)}(x_i, t) \quad \text{for} \quad t > t_0^{(M)} \quad \text{and} \quad M \leq N, \tag{4}$$

where

$$\tilde{T}^{(I)}(x_i, t) = \frac{Q^{(I)} A}{4\rho c_p \left(\pi\alpha \left(t - t_0{}^{(I)}\right)\right)^{3/2}} \exp\left(\frac{-\left(R^{(I)}\right)^2}{4\alpha\left(t - t_0{}^{(I)}\right)}\right). \tag{5}$$

Granted $t \geq t_0^{(I)}$, Eq. (5) is the analytical solution of the linear heat equation Eq. (2) for an instantaneous point source I in a semi-infinite medium which is bounded by the top surface of body ∂V_{top} [39]. If $t < t_0^{(I)}$, $\tilde{T}^{(I)}(x_i, t) = 0$. In Eq. (5), $Q^{(I)}$ represents the energy associated with source I. When the time step Δt is sufficiently small, $Q^{(I)} = P\Delta t$. Source I is created at time $t_0^{(I)}$ and $R^{(I)}$ is the distance between the material point of interest x_i and the source position $x_i^{(I)}$. We note in passing, Eq. (5) becomes singular exactly when the source is created, i.e., for $t = t_0{}^{(I)}$. In reality the laser spot has a finite radius r and in order to mimic this effect we introduce in Eq. (5) a time shift

$$\tau_0{}^{(I)} = t_0{}^{(I)} - \frac{r^2}{8\alpha} \tag{6}$$

and replace $t_0{}^{(I)}$ in Eq. (5) with $\tau_0{}^{(I)}$. This time shift implies a diffusion distance of r for the point source I and thus also eliminates the singularity in Eq. (5).

The influence of the finite dimensions of the powder bed and the associated boundary conditions are accounted for by the complimentary temperature field $\hat{T}$ which is governed by

$$\frac{\partial \hat{T}}{\partial t} = \alpha \nabla^2 \hat{T} \qquad \text{in} \quad V, \tag{7a}$$

with boundary conditions

$$\hat{T} = T_c - \tilde{T} \qquad \text{on} \quad \partial V_{\text{bot}}, \tag{7b}$$

$$\frac{\partial \hat{T}}{\partial x_i} n_i = -\frac{\partial \tilde{T}}{\partial x_i} n_i \qquad \text{on} \quad \partial V_{\text{lat}} \quad \text{and}, \tag{7c}$$

$$\frac{\partial \hat{T}}{\partial x_i} m_i = -\frac{\partial \tilde{T}}{\partial x_i} m_i = 0 \qquad \text{on} \quad \partial V_{\text{top}}, \tag{7d}$$

where n_i and m_i are the outward facing normal to ∂V_{lat} and ∂V_{top}, respectively. Eq. (7d) is a direct consequence of the no flux condition on ∂V_{top} implicit in the solution of $\tilde{T}$. The initial condition at $t = 0$ reads

$$\hat{T}(x_i, 0) = T(x_i, 0) - \tilde{T}(x_i, 0), \tag{7e}$$

where $\tilde{T}(x_i, 0)$ is obtained by Eq. (4) and in the present paper, the initial temperature $T(x_i, 0)$ is assumed to be equal to the chamber temperature T_c.

Provided $\tilde{T}$ and its gradient are finite on $\partial V_{\text{lat}} \cup \partial V_{\text{bot}}$, Eq. (7) is a smooth problem that can be solved by a standard numerical method such as finite differences and the wavelengths associated with the $\hat{T}$ field scales with the dimensions of the body. However, for a point source created at a location sufficiently close to the boundary $\partial V_{\text{lat}} \cup \partial V_{\text{bot}}$, Eq. (5) implies that the wavelengths associated with the solution of $\hat{T}$ become comparable with that of $\tilde{T}$. This in turn requires a discretisation on the order of the laser spot radius r for $\hat{T}$ and thus makes the solution of Eq. (7) computationally intractable. Therefore a special treatment is required for point sources within a critical distance from the boundary $\partial V_{\text{lat}} \cup \partial V_{\text{bot}}$. For this reason $\breve{T}$ field is introduced and the image point sources explained in the next section are utilised to analytically enforce boundary conditions for those sources located within a critical distance from the boundary $\partial V_{\text{lat}} \cup \partial V_{\text{bot}}$. The decomposition of total temperature given in Eq. (3) is modified as

$$T = \tilde{T} + \hat{T} + \breve{T}, \tag{8}$$

in the presence of the $\breve{T}$ field.

2.2. Image fields for heat sources

The basic principle of the image source method for three simple 2D geometries is illustrated in Fig. 4. By mirroring the original source I with respect to boundary $\partial B^{(1)}$ /$\partial B^{(2)}$, image source $J = 1/J = 2$ is created. If the energy associated with image source $J = 1$ is taken identical to the energy of the regular source I, $Q^{(I)}$, the heat flux at $\partial B^{(1)}$ due to the source I and the image source $J = 1$ is zero, while if the energy of the image source $J = 1$ is $-Q^{(I)}$ (negative energy implies a heat sink), the temperature at $\partial B^{(1)}$ due to the source I and the image source $J = 1$ is zero. The same relation also holds for the image source $J = 2$ and the boundary $\partial B^{(2)}$. At a first glance this suggests the boundary conditions given in Eqs. (1b)-(1d) can thus be satisfied by adding image sources only. However, the existence of the image source $J = 2$ infringes with the boundary condition at $\partial B^{(1)}$, and hence a second order reflection, i.e., a second order image source for the image source $J = 1$ is required. In

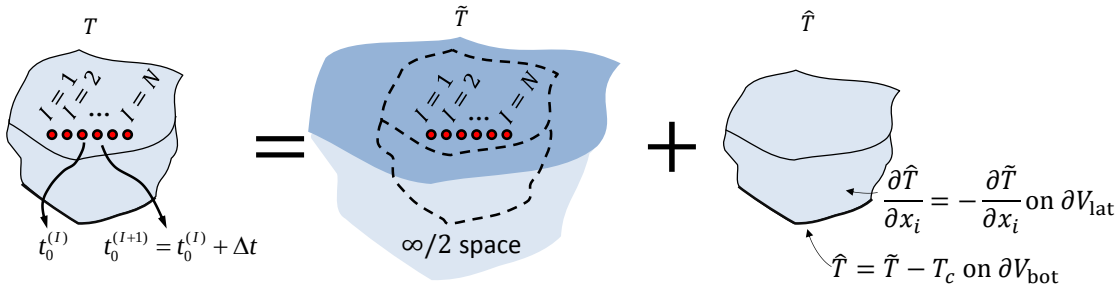

Figure 3: Decomposition of the thermal BVP with N point sources into the problem of heat sources in a semi-infinite space and the complementary BVP without the heat sources which accounts for the proper boundary conditions.

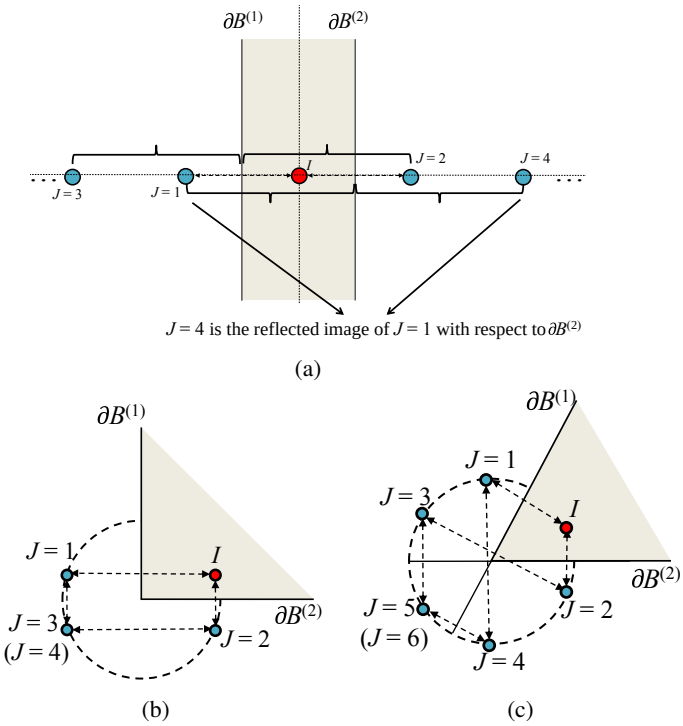

Figure 4: Schematic illustration of image source method in 2D examples. The regular source is indicated with a red point while the images sources are indicated with blue points. In (a) boundaries $\partial B^{(1)}$ and $\partial B^{(2)}$ are parallel to each other, $J = 1$ and $J = 2$ are first order image sources for the regular source I with respect to $\partial B^{(1)}$ and $\partial B^{(1)}$, respectively. The second order image source $J = 3$ is the image of $J = 2$ reflected with respect to $\partial B^{(1)}$, while $J = 4$ is the image of $J = 1$ reflected with respect to $\partial B^{(2)}$. Since there is no bound on the order of reflection in this geometry, an infinite number of image sources is needed. In (b) boundaries $\partial B^{(1)}$ and $\partial B^{(2)}$ are orthogonal to each other, and a single second order image source, $J = 3$ suffice. In (c) the angle between the boundaries $\partial B^{(1)}$ and $\partial B^{(2)}$ is less than 90°, and two second order image sources with $J = 3$ and $J = 4$ and a single third order image source with $J = 5$ are required. (For interpretation of the references to colour in this figure legend, the reader is referred to the web version of this article.)

Fig. 4b the image source with index $J = 3$ is an example of a second order image source which is the mirror image of image source $J = 2$ with respect to $\partial B^{(1)}$. Similarly, for the boundary $\partial B^{(2)}$, a second order image source which is the mirror image of image source $J = 1$ with respect to $\partial B^{(2)}$ is required. It can be observed from Fig. 4b, orthogonality of $\partial B^{(1)}$ and $\partial B^{(2)}$, yields a single second order image source $J = 3$ to be sufficient. In Fig. 4c, two second order image sources, i.e., $J = 3$ and $J = 4$ and a single third order image source with an index $J = 5$ is required. Finally for the two parallel boundaries shown in Fig. 4a, an infinite number and order of image sources is necessary.

Generally, for a 3D BVP with N regular sources, either infinitely many or a large number of image sources are required to satisfy the boundary conditions given in Eqs. (1b)-(1d). Even if the geometry dictates a finite number of image sources such as the 2D examples depicted in Fig. 4b and c, the computational costs increase as the number of image sources increases [40]. However, it can also be observed that as the order of reflection increases, the distance between the boundary and image source also increases (see Fig. 4). Consequently, the temperature field due to higher order image sources will be sufficiently smooth at the boundary and thus can be accounted in the numerical solution of $\hat{T}$. In this way a limited number of image sources is introduced only when the distance between the regular or image source being mirrored and the boundary of interest is less than a critical distance H_c. Otherwise the boundary correction is enforced by the $\hat{T}$ field only.

The temperature field $\breve{T}$ due to all image sources is represented by

$$\breve{T} = \sum_{I=1}^{N} \sum_{J=1}^{N_I} \breve{T}^{(J)}, \tag{9}$$

where N_I is the total number of image sources associated with regular source I, and $\breve{T}^{(J)}$ is the temperature field due to a point image source J where $J = 1, \ldots N_I$. When $t \geq t_0^{(I)}$, similar to $\tilde{T}^{(I)}$, $\breve{T}^{(J)}$ is expressed as

$$\breve{T}^{(J)}(x_i, t) = \frac{Q^{(J)} A}{4\rho c_p \left(\pi\alpha \left(t - \tau_0{}^{(I)}\right)\right)^{3/2}} \exp\left(\frac{-\left(R^{(J)}\right)^2}{4\alpha \left(t - \tau_0{}^{(I)}\right)}\right) \tag{10}$$

where $R^{(J)}$ is the distance between the material point of interest x_i and the image source position $x_i^{(J)}$. For the image sources

reflected by ∂V_{lat}, the energy of the image source $Q^{(J)}$ is equal to $Q^{(I)}$, whereas for the image sources reflected by ∂V_{bot}, $Q^{(J)}$ is equal $-Q^{(I)}$, i.e., these act as point heat sinks. It is worth emphasising the use of image fields is suitable only if the body V is a convex polyhedron (where any two points within the polyhedron can be connected by a line) which we exclusively consider in the remainder of the paper.

The complimentary temperature field $\hat{T}$ is still governed by Eq. (7a). However, according to Eq. (8), the boundary conditions are now modified as

$$\hat{T} = T_c - \tilde{T} - \breve{T} \qquad \text{on} \quad \partial V_{\text{bot}}, \quad \text{and,} \tag{11a}$$

$$\frac{\partial \hat{T}}{\partial x_i} n_i = -\frac{\partial \tilde{T}}{\partial x_i} n_i - \frac{\partial \breve{T}}{\partial x_i} n_i \qquad \text{on} \quad \partial V_{\text{lat}}. \tag{11b}$$

with the initial condition

$$\hat{T}(x_i, 0) = T(x_i, 0) - \tilde{T}(x_i, 0) - \breve{T}(x_i, 0), \tag{12}$$

where $T(x_i, 0) = T_c$.

Recall that the gradients in the $\tilde{T}$ and $\breve{T}$ fields diminish rapidly away from the source in the spatial domain. Consequently, we limit the number of image sources by not only the critical distance H_c consideration described above, but also with a temporal consideration. The gradients in the $\tilde{T}$ and $\breve{T}$ fields also diminishes with time, i.e., temperature field spreads away, c.f. Eq. (10). Thus, after a critical time t_c is elapsed after source I is created, we anticipate the $\tilde{T}^{(I)}$ and $\breve{T}^{(J)}$ fields for $J = 1, \ldots, N_I$ to be sufficiently smooth and hence can be well represented within the $\hat{T}$ field. Consequently, when $t > t_c$, source I and all the image sources associated with source I: $J = 1, \ldots, N_I$ are deleted and their contribution to the total temperature is transferred to $\hat{T}$ as

$$\hat{T} := \hat{T} + \tilde{T}^{(I)} + \sum_{J=1}^{N_I} \breve{T}^{(J)}. \tag{13}$$

The critical spreading time is taken to be $t_c = t_0^{(I)} + (pl_e)^2/4\alpha$ where l_e is the finite difference cell size used in solving $\hat{T}$ and p is a numerical parameter to be determined. The efficiency of the proposed model is further improved by eliminating regular and image sources that have spread out.

We note in passing, although the laser is discretised as point heat sources, it is possible to consider Gaussian surface sources or even volumetric sources. Yang and Ayas [41] compared the temperature fields obtained by treating laser scanning vectors as a set of point, surface and volumetric sources. For process parameters identical to the present study, it is found that when the laser spot radius is 35 μm, the resultant temperature fields dictated by these three different type of sources are virtually identical even at the close vicinity of the source location at all times [41]. Consequently, in this paper scanning vectors are described by a set of point sources to enhance the computational efficiency of the simulation.

In conclusion, the assumption of an semi-infinite space considered for $\tilde{T}$ field does not influence the accuracy of the total solution, i.e., the combination of the analytical solution $\tilde{T}$ plus the corresponding corrections $\hat{T}$ and $\breve{T}$ indeed satisfies the correct boundary conditions which, of course, reflect the geometric complexity and the finite dimensions of the product at hand.

3. Validation

In this section, we analyse the temperature-time evolution due to a single laser scan vector applied on a semi-infinite solid and compare our predictions with relevant experimental findings reported in [42]. Since in our formulation, a laser scan vector is represented with a number of point sources which is controlled by the time step Δt we shall determine:

(i) the appropriate time step Δt for the discretisation of laser scanning and,

(ii) the appropriate values of material properties that are deemed temperature independent in the current linear framework.

Finally, a thermal problem with known analytical solution is studied aiming to determine the fidelity of the $\hat{T}$ and $\breve{T}$ fields for imposing boundary conditions.

3.1. Laser scanning on a semi-infinite plate

Wits *et al.* [42] built single lines of Ti-6Al-4V alloy with SLM on a large base plate of the same alloy. The dimensions of the base plate were length L_l =30 mm, width L_w =30 mm and depth L_d =5 mm, while laser scan vectors of 6.5 mm with laser spot radius of 35 μm were applied on a powder layer with a thickness of 50 μm. Neighbouring lines were built sufficiently apart in order to ensure the temperature field associated with a previously built line had no effect on the current line. The produced samples were cut across and inspected with a microscope and the measured melt-pool dimensions along the line were reported for a range of SLM process parameters.

We consider the large base plate of Ti-6Al-4V alloy schematically shown in Fig. 5 and a single laser scan vector applied to build a 6.5 mm long line. Since the above quoted dimensions of the base plate are much larger than the corresponding dimensions of the line built, we treat the base plate as a semi-infinite solid. The time evolution of the temperature field is then directly predicted as

$$\begin{aligned} T(x_i, t) &= \sum_{I=1}^{M} \tilde{T}^{(I)}(x_i, t) \\ &= \frac{P \Delta t A}{4 \rho c_p \, (\pi \alpha))^{3/2}} \sum_{I=1}^{M} \frac{\exp\left(\frac{-(R^{(I)})^2}{4\alpha(t-\tau_0^{(I)})}\right)}{(t - \tau_0^{(I)})^{3/2}}, \end{aligned} \tag{14}$$

while $\hat{T}$ and $\breve{T}$ fields have zero contribution. [2] Here $\tilde{T}^{(I)}$ is the temperature field associated with the point source I given by Eq. (5) with $Q^{(I)}$ explicitly given as $P\Delta t$.

[2] Previously we have explained that it is customary to impose a temperature boundary condition at interface between the body and the base plate. However, for the first few layers of the built the temperature of base the plate indeed increases because of the close proximity of scanning vectors. That is why the temperature boundary condition $T = T_c$ is not imposed in Section 3.1

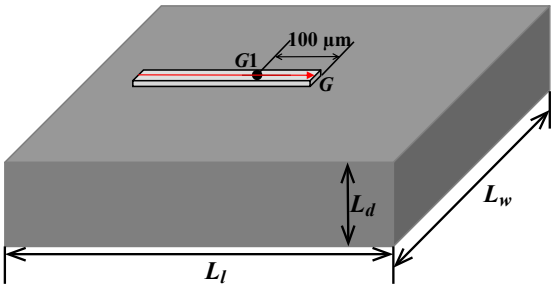

Figure 5: A schematic illustration of a single scanning vector indicated with a red arrow applied on a large base plate and the resulting material built. At a certain moment, the laser reaches Point G. The point labelled with G1 is located on the scanning vector and has a distance of 100 μm to Point G. The temperature of Point G1 is used to investigate the convergence of the proposed model. (For interpretation of the references to colour in this figure legend, the reader is referred to the web version of this article.)

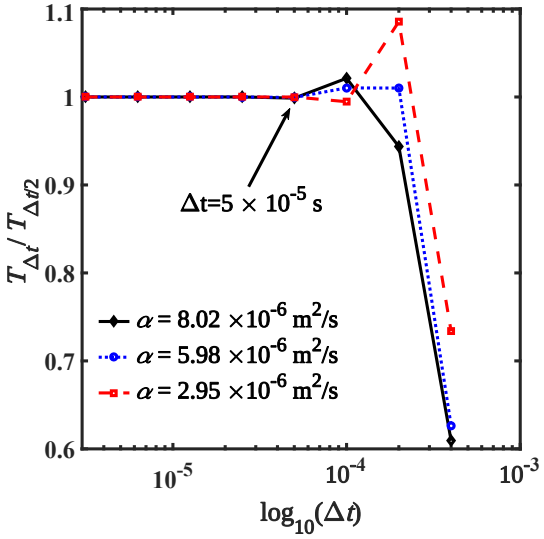

Figure 6: Temporal convergence behaviour of temperature for Point G1. $T_{\Delta t}$ is the temperature at Point G1 when the laser reaches Point G with the time step Δt, while $T_{\Delta t/2}$ is the temperature calculated with the time step $\Delta t/2$.

We consider the time when the the laser arrives at Point G which marks the end of the single scan vector applied (see Fig. 5). The non-dimensional parameter $T_{\Delta t}/T_{\Delta t/2}$, which represents the temperature field $T_{\Delta t}$ calculated with a time step Δt divided by the temperature field $T_{\Delta t/2}$ calculated with a time step $\Delta t/2$ is studied to evaluate the temporal convergence behaviour of T. From Eq. (14), it can be inferred that $T_{\Delta t}/T_{\Delta t/2}$ depends on (i) the distance between the point of interest and the source positions $R^{(I)}$ [3] and (ii) the thermal diffusivity α. In Fig. 6, $T_{\Delta t}/T_{\Delta t/2}$ is given as a function of Δt at point G1 on the scanning vector located 100 μm away from the Point G (see Fig. 5). Since the thermal diffusivity α for Ti-6Al-4V ranges between 2.95×10^{-6}–8.02×10^{-6} m^2/s as a function of temperature [43], results are plotted for the selected values of α. The convergence is attained for $\Delta t = 0.5 \times 10^{-4}$s irrespective of the chosen α value. Therefore, this time step will be used in the remainder of the paper. Convergence has been analysed also for various material points other than G1 and all exhibited convergence for $\Delta t = 0.5 \times 10^{-4}$s.

It remains to calculate the melt pool width w, i.e., the width of material points around the scan vector heated above the melting point (T_m = 1928 K) at the top surface of the base plate. However, note that Eq. (14) is based on the linear heat equation and requires the material parameters ρ, c_p and k to be temperature independent whereas, in reality, heat capacity c_p and the conductivity k have a significant temperature dependence. Therefore the thermal material properties in our model are determined upon comparing model predictions with the experimental measurements and FE predictions of Wits *et al.* [42]. In Fig. 7, melt-pool width w is plotted against energy density P/v for selected values of P. It is found that the melt pool width, predicted with the material properties listed in Table. 1 yields the best agreement with the experimental measurements of Wits *et al.* [42]. The thermal material properties tabulated in Table 1 correspond to a temperature value of 2500 K [44] which is above the melting point. This is consistent with the fact that material points determining the width of the melt-pool being indeed around or above the melting point; see also [19] for a similar consideration. It is important to note that for $\alpha = 9.60\times10^{-6}$m^2/s corresponding to the temperature 2500 K, convergence is still achieved with the reference time step value $\Delta t = 5 \times 10^{-5}$s. It is important to note that for different energy densities and laser power values, good agreement between the model and the experimental data is observed in Fig. 7. However, for the laser power of 400 W, the highest value considered, model predictions overestimate the size of the melt-pool, when the energy density exceeds 600 J/m. This is most probably due to more pronounced convection and radiation at high power and high energy density conditions. As mentioned, these effects have been neglected in our model. Moreover, phase transitions – especially evaporation – are also expected to play a more important role at high power and energy densities [42]

Table 1: Determined material properties for the semi-analytical model.

Conductivity k (W/mK)	Heat capacity c_p (J/kgK)	Density ρ (kg/m^3)	Absorptivity fraction A (-)
42	990	4420	0.818

3.2. *Scanning on a finite domain*

Next, we consider the simplified problem of applying 20 *unidirectional* laser scanning vectors on a thermally insulated, cuboid body with the dimensions of $l_a = l_b = l_c = 2$ mm, as sketched in Fig. 8a, where the *unidirectional* scanning pattern is illustrated in Fig. 8b. A total of 20 scanning vectors each having a length of $l = 1.8$ mm are spaced apart with $h = 80\,\mu$m. Each scanning vector is discretised by an appropriate number of point sources. For a point source in an insulated cuboid, the exact solution of temperature field $T^{(I)}_{\text{exact}}$ is known [39] and given

[3] Note that $I = 1, \ldots, N$ while the number of sources N is now a function of time step Δt

Table 2: Process parameters

Laser power	Laser velocity	Laser spot radius	Chamber temperature	Scan vector length	Hatch spacing	Solid layer thickness
P (W)	v (m/s)	r (μm)	T_c (K)	l (mm)	h (μm)	d_s (μm)
35	0.3	35	453	1.8	80	100

in Appendix A. The infinite sums in Eq. (A.1) are approximated by taking $k = m = n = 100$. Consequently, the exact solution of the laser scanning problem at a material point of interest x_i can be attained by superposition,

$$T_{\text{exact}}(x_i) = \sum_{I=1}^{M} T^{(I)}_{\text{exact}}(x_i). \tag{15}$$

Finally, by means of comparing the exact solution with the predictions of the proposed semi-analytical scheme, the accuracy of the $\hat{T}$ and $\breve{T}$ fields can be analysed.

Next, we employ the semi-analytical model to the problem. In order to model a thermally insulated domain, a no heat-flux condition is imposed at ∂V_{bot} instead of the fixed temperature boundary condition described previously. Recall that a set of point sources represents the scanning vectors and in the semi-analytical model the temperature field is decomposed into the $\tilde{T}$, $\breve{T}$ and $\hat{T}$ fields as given in Eq. (8). For any material point x_i within the body, $\tilde{T}$ can be readily calculated using Eq. (4) and (5). We note in passing, the no-flux boundary condition at ∂V_{top} is implicit in Eq. (5). However, when the separation between a source and ∂V_{lat} is smaller than the critical distance [4] $H_c = 0.75$ mm, image source(s) are generated to partially impose the no-flux boundary condition. The selected value of H_c is approximately 21 times the spot radius r. The $\breve{T}$ solution is also calculated analytically at a material point of interest using Eq. (9) and (10). Finally, the solution of $\hat{T}$ is obtained with an explicit finite difference scheme, centred in space and forward in time. A total number of 64 cubic finite difference cells is used to discretise the body, resulting in a cell size of $l_e = 0.5$ mm, which is approximately 14 times of the spot radius r. The small number of cells used in turn is the key to the computational efficiency of the numerical solution and hence the semi-analytical scheme.

As explained above, $\tilde{T}$ can be readily calculated for any material point x_i within the body analytically while in contrast, the $\hat{T}$ field is computed and hence known only at the finite difference grid points, i.e., the nodes of the finite difference cells. Therefore, the value of $\hat{T}(x_i)$ on a material point x_i is estimated by a linear interpolation of known $\hat{T}$ values given by

$$\hat{T}(x_i) = \sum_{q=1}^{L} \Phi^{(q)} \hat{T}(x_i^{(q)}), \tag{16}$$

where $q = 1, \ldots, L$ is the index for the grid point with $\hat{T}(x_i^{(q)})$ and L is the total number of grid points of the finite difference cell which contains x_i. For an 8-node hexahedral finite difference cell ($L = 8$) used in this study, the interpolation function $\Phi^{(q)}$ for grid point q reads

$$\Phi^{(q)} = \frac{1}{8}(1 + \zeta_i \zeta_i^{(q)}), \tag{17}$$

where ζ_i is the normalised position of x_i in a right handed local coordinate system having an origin located at the center of the cell and $\zeta_i^{(q)}$ is the normalised position $x_i^{(q)}$ given in the same local coordinate system.

Regular and image sources that spread for a duration of $(pl_e)^2/4\alpha = 0.0146$ s with $p = 1.5$ are deleted and their contribution to the total temperature is transferred to $\hat{T}$ in accordance with Eq. (13). For the finite difference cell size $l_e = 0.5$ mm, the time step $\Delta t = 5 \times 10^{-5}$ s ensures the numerical stability of the explicit finite difference scheme ($3\alpha\Delta t/l_e^2 < 1/2$). For the sake of completeness, the material properties and process parameters are listed in Table 1 and Table 2, respectively.

The temperature history predicted by the semi-analytical model, at Point A (shown in Fig. 8b), normalised with melting temperature T_m is plotted in Fig. 9. The exact solution T_{exact} at Point A normalised with T_m is also included in Fig. 9. Perfect agreement between the two solutions is observed, demonstrating the fidelity of the $\hat{T}$ and $\breve{T}$ fields to impose boundary conditions with the given numerical parameters. It can be observed from Fig. 8b that boundary conditions has a pronounced effect on the temperature at point A. This due to given proximity of point A to the surface of the body. Comparing the exact and semi-analytical solution at various different points also yielded a perfect agreement.

We end this section with another case study reminiscent to the one discussed in Section 3.1 where a single laser track is scanned directly on a Ti-6Al-4V base plate with length $L_l = 4$ mm, width $L_w = 2$ mm and depth $L_d = 0.5$ mm, see Fig.5. Fu and Guo [45] built a single line along the length direction of the base-plate using a powder layer thickness of 30 μm. A fixed laser speed of 0.2 m/s was used but the laser power was varied in the range of 20 to 80 W and the corresponding melt-pool width was measured. In Fig. 10, melt-pool width as reported by Fu *et al.* [45] is given along with the predictions of the semi-analytical model. The error bars of the experimental data denote the variation in measurement. Since the dimensions of the base plate are relatively small, in contrast to the case study described in Section 3.1 where the base plate is considered as a semi-infinite space, here it is appropriate to consider the base-plate as the body under consideration V, c.f. Fig. 2a. Consequently, we make use of the image sources and the complimentary numerical correction field to account for the boundary conditions ($T = 20$ °C at the bottom surface and no heat flux at

[4] The value of H_c has been determined by analysing the accuracy of $\hat{T}$ for a source located close to a boundary

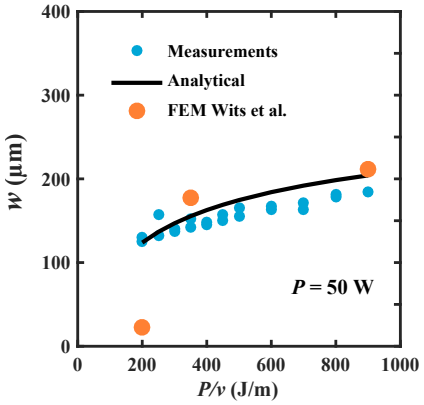

(a)

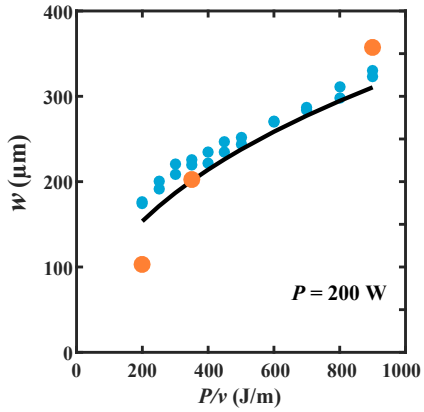

(b)

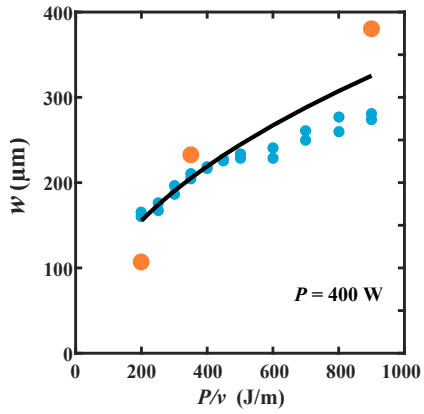

(c)

Figure 7: The melt-pool width w as a function of the energy density P/v for a laser power of (a) $P = 50$ W (b) $P = 200$ W (c) $P = 400$ W. The results predicted by the analytical solution of Eq. (14) are given along with the experimental measurements and FE predictions reported by Wits *et al.* [42].

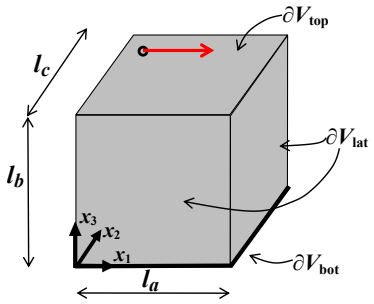

(a)

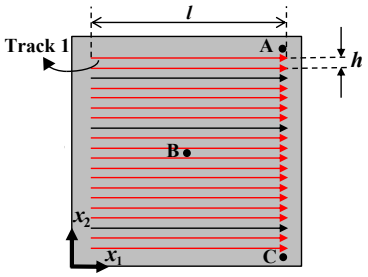

(b)

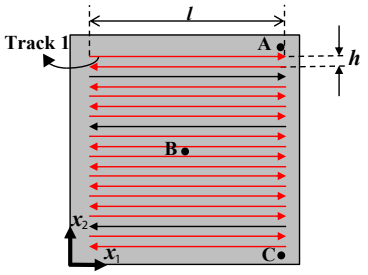

(c)

Figure 8: (a) Schematic representation of body V where scanning vectors are applied to its top surface ∂V_{top} with (b) a *unidirectional* scanning pattern and with (c) a *zigzag* scanning pattern. The coordinates of the points labelled with A, B and C, given in terms of mm are (1.9, 1.8, 2), (1, 1, 2), (1.9, 0.2, 2), respectively. The temperature field and the dimension of the melt-pool will be studied when the laser scans the 3$^{\text{rd}}$, 8$^{\text{th}}$ and 18$^{\text{th}}$ track, which are plotted as the black lines.

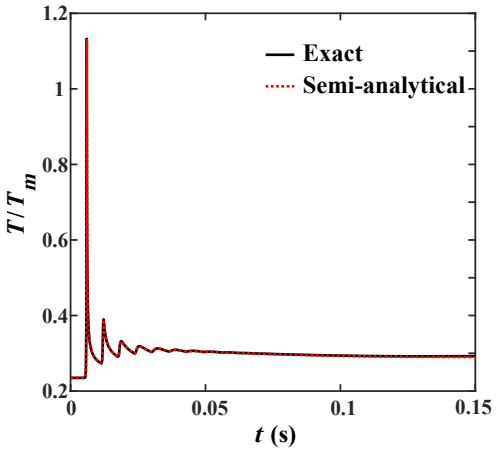

Figure 9: Normalised temperature T/T_m at Point A given in Fig. 8 is plotted as function of temperature. The temperature predicted by the semi-analytical model is in perfect agreement with the exact solution.

the lateral surfaces of the base plate [45]). The cell size l_e, time step Δt and critical distance H_c for image sources are the same as the case study shown in Fig. 8. The absorptivity fraction is calculated to be 0.77 according to [19] for a powder layer thickness of 30 μm and the thermal properties tabulated in Table. 1 were used in the calculations. Good agreement between the experimental findings and the model predictions are observed in Fig. 8 which further validates the fitting described in Section 3.1 for the temperature dependent material parameters.

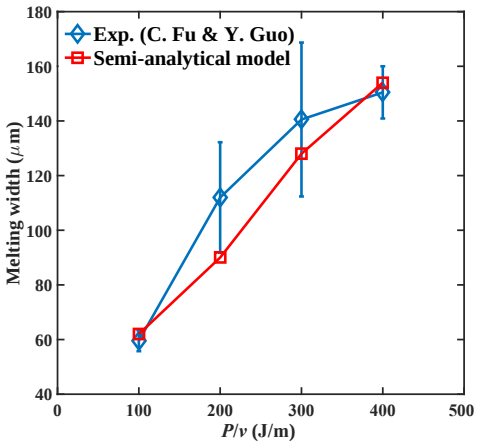

Figure 10: The melt-pool width w as a function of the energy density P/v. The results predicted by the semi-analytical model are given along with the experimental measurements by Fu and Guo [45].

4. Process modelling of SLM

In Section 3.1, we were able to capture the essential thermal phenomena taking place during SLM by way of discretising a laser scan vector into point sources. Subsequently in Section 3.2, the accuracy of the numerical scheme with image source considerations of the semi-analytical approach were validated. We now proceed with employing the semi-analytical approach to problems more closely related to the actual SLM process and investigate modelling of (i) building a single layer and (ii) building multiple layers of a body while keeping all the process parameters fixed to their reference values given in Table 2.

As described in the previous section, hexahedral finite difference cells with 8 grid points are used to resolve the $\hat{T}$ field. For the single layer calculations, cubic finite difference cells with a length of $l_e = 0.5$ mm is used. Recall that in Section 3.2, it was demonstrated this mesh size gives the desired level of accuracy. For the multilayer calculations, finite difference cells with a thickness 0.1 mm are adopted such that each new layer with a thickness of 0.1 mm is one finite difference cell thick, whereas the other dimensions of the cells are kept at 0.5 mm.

4.1. Building a single layer

We consider the 2 mm × 2 mm × 2 mm cube described in Section 3.2 and illustrated in Fig. 8a which is bonded on a base plate across ∂V_{bot}. Temperature is fixed to the chamber temperature, i.e., $T = T_c$ at the bottom surface ∂V_{bot}, while a no flux boundary condition is imposed on the remaining surfaces, i.e., $\partial V_{\text{lat}} \cup \partial V_{\text{top}}$. Building of an additional layer on top of the existing body is by applying two different scanning patterns: *unidirectional* scanning and *zigzag* scanning, as shown schematically in Fig. 8b and Fig. 8c, respectively. A total of 20 scanning vectors, each having a length of $l = 1.8$ mm that are spaced apart $h = 80$ μm are applied. Since all the process parameters are fixed to their reference values, the effect of two different scanning patterns on the temperature history and melt-pool dimensions are investigated.

The normalised temperature T/T_m distributions on the surface ∂V_{top} at selected time instances of the building process are shown in Fig. 11a–c for the *unidirectional* scanning pattern and Fig. 12a–c for the *zigzag* scanning patterns. The temperature fields shown in Fig. 11a, b and c are given for time instances corresponding to completion of scanning tracks drawn in black in Fig. 8b while the temperature fields shown in Fig. 12a, b and c are given for time instances corresponding to completion of scanning tracks drawn in black in Fig. 8c. Similarly, normalised temperature T/T_m distributions at above described time instances, on the $x_1 - x_3$ plane at various cross-sections are shown in Fig. 11d – f for the *unidirectional* scanning pattern and in Fig. 12d – f for the *zigzag* scanning pattern. Local melting in the vicinity of the laser spot is observed from Fig. 11 and Fig. 12. The molten material subsequently solidifies rapidly as the laser spot moves away. When the 3$^{\text{rd}}$ scanning vector is completed, i.e., when $t = 0.018$ s (see Fig. 11a and d and Fig. 12a and d) the body is by enlarge at its initial temperature T_c, irrespective of the scanning pattern. When the 18$^{\text{th}}$ scan vector is applied at $t = 0.108$ s, (see Fig. 11c and f and Fig. 12c and f) the average temperature of the body is slightly increased, whereas the material points in the vicinity of the first few scan vectors cooled down to the initial temperature.

The normalised temperature T/T_m at Point B and Point C, (as shown in in Fig. 8b and c, respectively) are plotted as a function

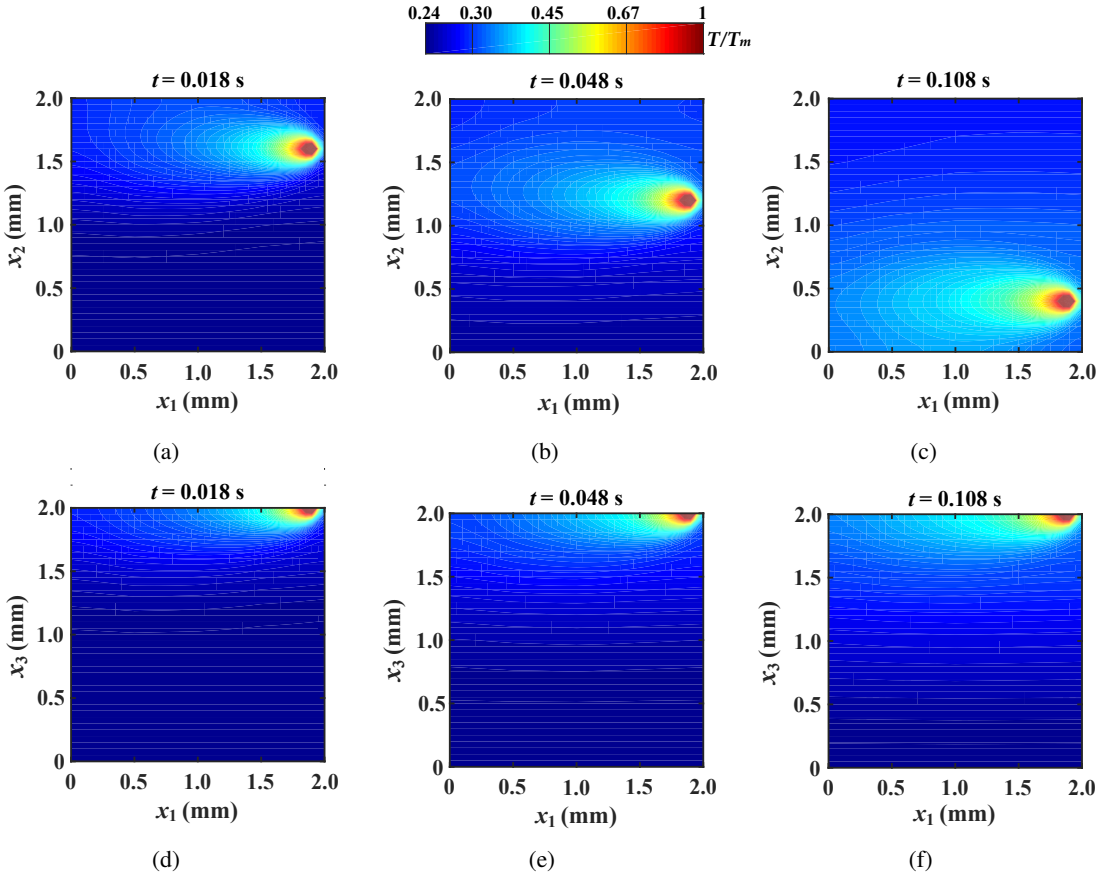

Figure 11: Snapshots of normalised temperature T/T_m distribution in the $x_1 - x_2$ plane (top row) and in the $x_1 - x_3$ plane (bottom row) at (a) and (d) t = 0.018 s corresponds to the end of 3rd scan vector (b) and (e) t = 0.048 s corresponds to the end of 8th scan vector and (c) and (e) t = 0.108 s corresponds to the end of 18th scan vector. For (a), (b) and (c) x_3 = 0 while for (d) x_2 = 1.6 mm, (e) x_2 = 1.2 mm and (f) x_2 = 0.4 mm. All the results are for the *unidirectional* scanning pattern.

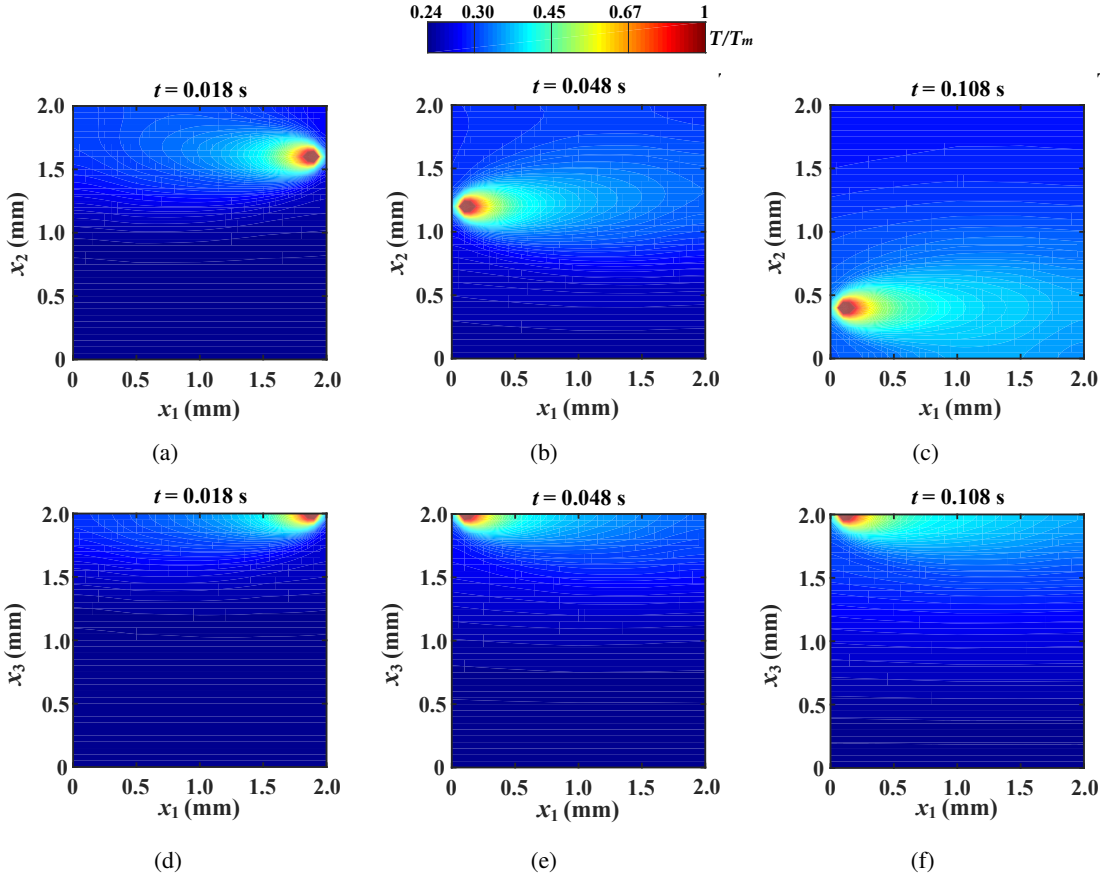

Figure 12: Snapshots of normalised temperature T/T_m distribution in the $x_1 - x_2$ plane (top row) and in the $x_1 - x_3$ plane (bottom row) at (a) and (d) $t = 0.018$ s corresponds to the end of 3rd scan vector (b) and (e) $t = 0.048$ s corresponds to the end of 8th scan vector and (c) and (e) $t = 0.108$ s corresponds to the end of 18th scan vector. For (a), (b) and (c) $x_3 = 0$ while for (d) $x_2 = 1.6$ mm, (e) $x_2 = 1.2$ mm and (f) $x_2 = 0.4$ mm. All the results are for the *zigzag* scanning pattern.

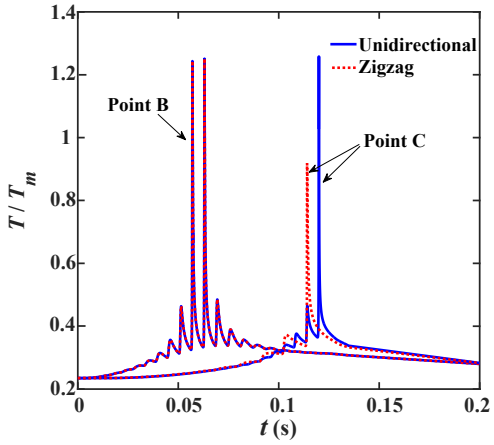

Figure 13: Prediction of temperature history of Point B and Point C for *unidirectional* and *zigzag* scanning patterns.

of time in Fig. 13. Since Point B is located at the center of ∂V_{top} and in between two adjacent scan vectors, temperature history of Point B is identical for the two scanning patterns considered. Two distinct temperature peaks are observed corresponding to the 10^{th} and the 11^{th} scan vectors that are passing near Point B. For Point C, the peak temperature is attained at a later stage as anticipated.

It is important to investigate the melt-pool dimensions since this is an important quality indicator for the product being built. For this purpose we determine the melt-pool dimensions around each scanning vector by way of monitoring the maximum width w and depth d of the material points that are above T_m. In Fig. 14 the melt-pool width w and depth d are depicted as a function of the x_1 coordinate, at selected instances of the process, for the two different scanning patterns. For the *unidirectional* scanning pattern, as shown in Fig. 14a and b, the melt-pool width and depth are small at the beginning of each scanning vector but quickly reach a higher steady-state value and subsequently diminish as the scanning vector is close to completion. The smaller melt-pool dimensions in the beginning and towards the completion of a scan vector can be rationalised as follows. Consider a material point x_i^p located on the trajectory of a scan vector where melt-pool dimensions w and d are being determined. As the laser spot is approaching towards x_i^p, the temperature starts to increase and a melt-pool starts to form when temperature surrounding x_i^p exceeds T_m. Melt-pool dimensions w and d keep increasing as the laser spot reaches to x_i^p and the melt-pool dimensions reach their maximum slightly after the laser passes x_i^p. Therefore the temperature of x_i^p is increasing both when the laser beam is approaching to and distancing away from x_i^p. Consequently, smaller melt pool dimensions are observed towards the start and end of scan vectors.

Overall melt-pool dimensions increase for *unidirectional* consecutive scan vectors as the layer being built approaches completion. This is caused by the increase in average temperature of the body with more of the laser scan vectors being applied. A similar trend of an increase (at least in peak values) of melt-pool dimensions occurs when successive scan vectors are applied in the *zigzag* scanning pattern where the amount of increase in melt-pool dimensions is more pronounced as depicted in Fig. 14c and d. However, the typical development of w and d across the x_1 coordinate shows that the maximum melt-pool dimensions are attained soon after the beginning of each scan vector. This is because of the nature of the *zigzag* scanning pattern. At the beginning of a current scanning vector trajectory, heating is prominent since the effect of the previous scan vector is still significant.

4.2. Building multiple layers

In this section, we model building multiple SLM layers on a 2 mm × 2 mm × 0.6 mm body as sketched in Fig. 15a that is attached to a base plate at its bottom surface. The total height of the body will reach 2 mm after building 15 layers with a thickness of 0.1 mm each. Building of the first layer is essentially laser scanning of the top surface with the semi-analytical model as discussed in the previous section. However, once scanning of the layer is completed, the top surface ∂V_{top} shifts up such that the modelled domain is extended, i.e., a new layer of finite difference cells is introduced. During the SLM process, prior to the laser scanning of a layer, a new layer of powder is laid down with a recoater which typically takes around 10 s [46]. Given the high conductivity of a solid metal, during the powder recoating, solid can cool down to its initial temperature. In Section 4.1 a single layer simulation showed that the temperature throughout the body of dimensions 2 mm × 2 mm × 2 mm cools down to its initial temperature T_c in only 0.88 s. Therefore, it suffices to assume a recoating time of 0.88 s for the geometry considered. The duration of laser scanning of a 2 mm × 2 mm layer depicted in Fig.8 is 0.12 s with a scan speed of $v = 300$ mm/s.

Two scanning strategies denoted as *fixed* and *alternating* are considered using a *unidirectional* scanning pattern. In the *fixed* scanning strategy, the direction of the scan vectors in consecutive layers denoted by $i = 1, \ldots, 15$ are shown in Fig. 15b. In the *alternating* scanning strategy odd numbered layers have the identical scanning pattern of the *fixed* scanning strategy whereas scan vectors are rotated by 90° in clockwise direction for even numbered layers as shown in Fig. 15c.

The temperature history in terms of normalised temperature T/T_m at Point $\text{C}^{(i)}$ on layer i is given for *fixed* and *alternating* scanning strategies in Fig. 16a and Fig. 16b, respectively. For the *fixed* scanning strategy, the evolution of temperature at Point $\text{C}^{(i)}$ on different layers are similar albeit the value of the peak temperature increases slightly as the number of layers built increases (see Fig. 15a). The peak value of temperature at Point $\text{C}^{(i)}$ for the whole scanning process, T_{peak} is plotted against time in Fig. 16c for both scanning strategies considered. It is observed that for the *fixed* scanning strategy, T_{peak} increases for the first few layers deposited but then reaches to a plateau value. We rationalise the increase by observing that if the distance between the uppermost layer and the base plate is small, the $T = T_c$ boundary condition imposed on ∂V_{bot} lowers the peak temperature value attained at the top surface ∂V_{top}. It can be seen from Fig. 16(c) that for $i > 10$ the effect of the base plate which essentially functions as a heat sink ceases to affect the T_{peak} value. For the *alternating* scanning strategy, the

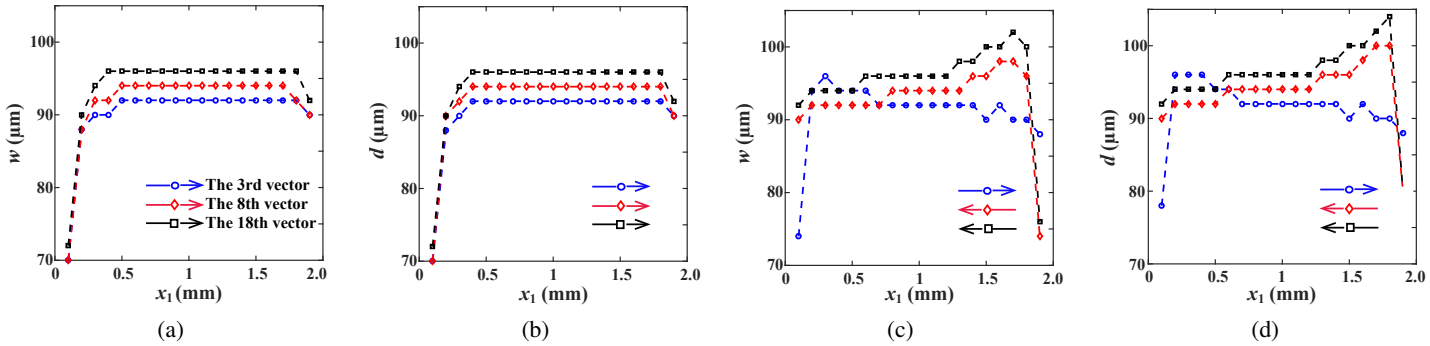

Figure 14: Melt-pool dimensions of the 3rd 8th, and 18th vector scans along the x_1 direction for (a) and (b) the *unidirectional* scanning pattern and for (c) and (d) the *zigzag* scanning pattern.

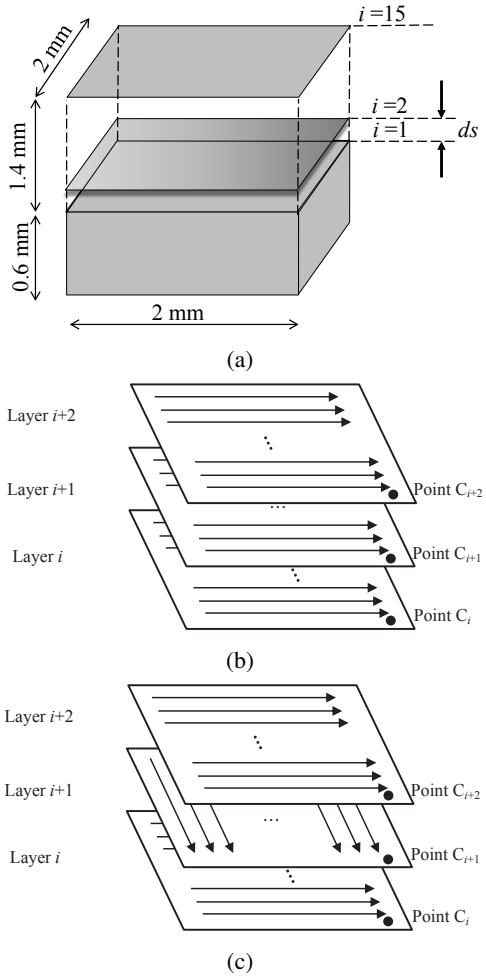

Figure 15: (a) Schematic illustration of (a) building 15 layers with a (b) fixed scanning strategy where the scanning directions are kept fixed for all the 15 layers and (c) alternating scanning strategy where the scanning pattern is rotated 90° in clockwise direction with respect to the scanning pattern of the previous layer.

Table 3: Computation time of the single layer build problem with 20 *unidirectional* scanning vectors with semi-analytical model.

Temperature fields	Computation time (s)
$\tilde{T}$	5.3
$\breve{T}$	7.5
$\hat{T}$	3.7
$T = \tilde{T} + \breve{T} + \hat{T}$	16.5

temperature history of Points $C^{(i)}$ at odd numbered layers are identical to those of the *fixed* scanning strategy. For even numbered layers, the peak temperature reduces significantly and it occurs for Point $C^{(i)}$ (where i is an even number) when the laser scans the next layer $i + 1$ (see Fig. 16b and c). This is because the distance between the last scanning vector of layer $i + 1$ and Point $C^{(i)}$ is smaller than the distance between the last scanning vector of the layer i and Point $C^{(i)}$.

For the current example, since all material points cool down to their initial temperature T_c after 0.88 s, the temperature field due to scanning of a particular layer is independent of the scanning of the previous ones. This implies that subsequent layers can be simulated in a parallel algorithm. In this way, increasing the number of layers will only result in a linear increase of the computational cost.

4.3. Computational cost

The CPU time of the single layer build problem as shown in Fig. 8b is determined in order to analyse the computational costs associated with the semi-analytical model. Here 20 *unidirectional* scanning vectors are applied on the top surface. Recall that dimensions of the model domain are 2 mm × 2 mm × 2 mm, the total vector length scanned is 36 mm and the total duration of the build was 1 s. For a finite cell size of $l_e = 0.5$ mm and a time step of $\Delta t = 5 \times 10^{-5}$ s, the total CPU time becomes 16.5 s [5] which can be further decomposed into computational time for calculating $\tilde{T}$, $\breve{T}$ and $\hat{T}$, as shown in Table. 3. It can be observed that the total time spent for the solution of the $\hat{T}$ fields

[5] Calculations are performed using a single-core Intel i7 - 6600U quad-core processor with a clock a speed of 2.60 GHz and with 8 GB RAM.

with the finite difference method is only around 22 % of the total CPU time. The relatively low computational time required for the numerical solution is due to the coarse finite difference grid that can be employed in the semi-analytical approach.

5. Conclusions

We have presented a semi-analytical method for modelling the thermal evolution of a body during SLM in a highly computationally efficient manner. The method relies on discretisation of laser scanning vectors using point heat sources. The temperature evolution is then computed by superposition of temperature fields due to sources (well-known in analytical form) and complimentary fields to enforce the boundary conditions. The complimentary fields comprise of image sources again with a known analytical solution and a smooth correction field that is solved by finite differences. Since the steep thermal gradients associated with the laser heating is accounted for analytically, the numerical solution can be accurately performed on a coarse finite difference grid. Consequently, the two key advantages of this new model are:

(i) computational costs of the thermal process simulations are extremely low, enabling simulations with multiple layers for macroscopic components with dimensions in the mm length scale;
(ii) the effect of different laser scanning patterns can be investigated since laser scanning vectors are explicitly modelled with a high level of accuracy.

Careful examination of the material and numerical parameters required for the semi-analytical model has been performed, so that a good match with experimental data from literature and exact solutions of simple problems are attained. The proposed model is also expected to be capable of modelling similar metal additive manufacturing process, such as direct energy deposition, because of similarity in boundary conditions. We envision the presented framework can be further utilised to predict the distortions and residual stresses that arise during the SLM processes upon coupling the present thermal model with a temperature dependent elasto-plastic mechanical model.

A limitation of the presented semi-analytical framework is also identified. Image fields can only be applied to bodies having convex surfaces only. Moreover, finding the necessary image sources and their locations easily becomes cumbersome for complex geometries. For these cases a pragmatic approach is to perform the boundary correction with the numerical solution of $\hat{T}$ fields only. A compromise between the level of accuracy and the computational efficiency determines the degree of spatial discretisation in the vicinity of the boundaries. Finite element implementation instead of the finite difference analysis is then more suitable which allows for mesh refinement in the vicinity of the boundaries.

In order to reduce the number of sources and thus required images, discretisation of the laser scan vectors can be performed using line heat sources instead of point sources. We anticipate a further increase in computational efficiency upon using line heat sources. The extension of the semi-analytical method using line heat sources is our current research focus and preliminary results can be found in [47].

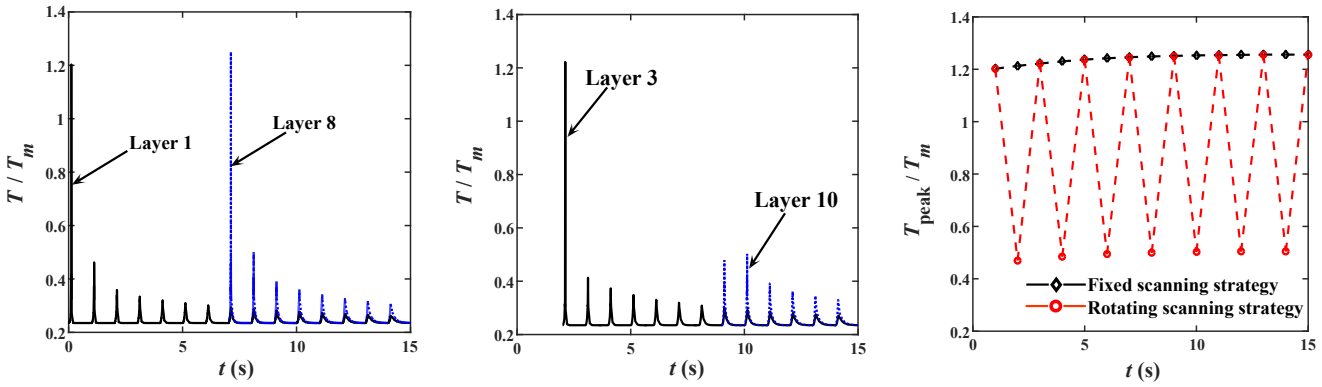

(a) (b) (c)

Figure 16: (a) normalised temperature T/T_m at Point C_i as a function of time (a) at layer $i = 1$ and $i = 8$ for *fixed* scanning strategy (b) at layer $i = 3$ and $i = 10$ for a *alternating* scanning strategy and (c) the peak normalised temperature for Point C_i at different layers for two scanning strategies.

Appendix A. Exact solution of a point source in an insulated cuboid

The analytical solution of the temperature field due to an instantaneous point source within an insulating cuboid is given by Carslaw and Jaeger [39] as

$$
\begin{aligned}
T(x_i,t) = {} & \frac{Q}{l_a l_b l_c \rho c_p} \times \\
& [1 + 2\sum_{m=1}^{\infty} \exp(-\alpha\pi^2(t-\tau_0)\frac{m^2}{l_a^2}) \cos(\frac{m\pi x_1}{l_a}) \cos(\frac{m\pi x_1'}{l_a})] \times \\
& [1 + 2\sum_{n=1}^{\infty} \exp(-\alpha\pi^2(t-\tau_0)\frac{n^2}{l_b^2}) \cos(\frac{n\pi x_2}{l_b}) \cos(\frac{n\pi x_2'}{l_b})] \times \\
& [1 + 2\sum_{k=1}^{\infty} \exp(-\alpha\pi^2(t-\tau_0)\frac{k^2}{l_c^2}) \cos(\frac{k\pi x_3}{l_c}) \cos(\frac{k\pi x_3'}{l_c})],
\end{aligned}
\tag{A.1}
$$

where l_a, l_b and l_c are the cuboid dimensions and x_i' is the location of the point source which is generated at $t = \tau_0$. For sufficiently high values of m, n and k, Eq. (A.1) can be regarded as the exact solution.

References

[1] I. Gibson, D. W. Rosen, B. Stucker, Additive Manufacturing Technologies, Springer, 2010.

[2] D. Thomas, The Development of Design Rules for Selective Laser Melting The Development of Design Rules for Selective Laser Melting, Ph.D. thesis, University of Wales Institute (2009).

[3] J. Gausemeier, Thinking ahead the Future of Additive Manufacturing Innovation Roadmapping of Required Advancements, Tech. rep., Direct Manufacturing Research Center (2013).

[4] J. P. Kruth, P. Mercelis, L. Froyen, M. Rombouts, Binding Mechanisms in Selective Laser Sintering and Selective Laser Melting, Rapid Prototyping Journal 11 (1) (2004) 26 – 36.

[5] B. Vandenbroucke, J.-P. Kruth, Selective laser melting of biocompatible metals for rapid manufacturing of medical parts, Rapid Prototyping Journal 13 (2007) 196–203.

[6] C. Casavola, S. L. Campanelli, C. Pappalettere, Preliminary investigation on distribution of residual stress generated by the selective laser melting process, The Journal of Strain Analysis for Engineering Design 44 (1) (2009) 93–104.

[7] L. Löber, C. Flache, R. Petters, U. Kühn, J. Eckert, Comparison of different post processing technologies for SLM generated 316l steel parts, Rapid Prototyping Journal 19 (2013) 173–179.

[8] U. Tradowsky, J. White, R. M. Ward, N. Read, W. Reimers, M. M. Attallah, Selective laser melting of AlSi10Mg: Influence of post-processing on the microstructural and tensile properties development, Materials & Design 105 (2016) 212–222.

[9] M. Langelaar, Topology optimization of 3d self-supporting structures for additive manufacturing, Additive Manufacturing 12, Part A (2016) 60 – 70.

[10] N. W. Klingbeil, J. L. Beuth, R. K. Chin, C. H. Amon, Measurement and Modeling of Residual Stress-Induced Warping in Direct Metal Deposition Processes, in: SFF Symposium, 1998, pp. 367–374.

[11] M. F. Zaeh, G. Branner, Investigations on residual stresses and deformations in selective laser melting, Production Engineering 4 (1) (2010) 35–45.

[12] I. Yadroitsev, I. Yadroitsava, I. Smurov, Strategy of fabrication of complex shape parts based on the stability of single laser melted track, in: W. Pfleging, Y. Lu, K. Washio (Eds.), SPIE–The International Society for Optical Engineering, Vol. 7921, 2011, pp. 79210C–79210C–13.

[13] H. Gong, K. Rafi, H. Gu, T. Starr, B. Stucker, Analysis of Defect Generation in Ti-6Al-4V Parts Made using Powder Bed Fusion Additive Manufacturing Processes, Additive Manufacturing (2014) 2–13

[14] P. Witherell, S. Feng, T. W. Simpson, D. B. Saint John, P. Michaleris, Z.-K. Liu, L.-Q. Chen, R. Martukanitz, Toward Metamodels for Composable and Reusable Additive Manufacturing Process Models, Journal of Manufacturing Science and Engineering 136 (6) (2014) 061025.

[15] S. Clijsters, T. Craeghs, J. P. Kruth, A priori process parameter adjustment for SLM process optimization, in: Innovative Developments in Virtual and Physical Prototyping - Proceedings of the 5th International Conference on Advanced Research and Rapid Prototyping, 2012, pp. 553–560.

[16] P. Yuan, D. Gu, Molten pool behaviour and its physical mechanism during selective laser melting of TiC/AlSi10Mg nanocomposites: simulation and experiments, Journal of Physics D: Applied Physics 48 (2015) 035303.

[17] L. Parry, I. A. Ashcroft, R. D. Wildman, Understanding the effect of laser strategy on residual stress in selective laser melting through thermo-mechanical simulation, Addtive Manufacturing 12 (2016) 1–15.

[18] J. Kruth, L. Froyen, J. Van Vaerenbergh, P. Mercelis, M. Rombouts, B. Lauwers, Selective laser melting of iron-based powder, Journal of Materials Processing Technology 149 (1-3) (2004) 616–622.

[19] A. V. Gusarov, I. Yadroitsev, P. Bertrand, I. Smurov, Model of Radiation and Heat Transfer in Laser-Powder Interaction Zone at Selective Laser Melting, Journal of Heat Transfer 131 (7) (2009) 072101.

[20] L. Papadakis, A. Loizou, J. Risse, J. Schrage, Numerical Computation of Component Shape Distortion Manufactured by Selective Laser Melting, Procedia CIRP 18 (2014) 90–95.

[21] B. Zeng, Kai, Teng, Chong, Xu, Sally, Sublette, Tim, Patil, Nachiket, Pala, Deepankar, Stucker, A Comparison of the Computational Speed of 3DSIM versus ANSYS Finite Element Analyses for Simulation of Thermal History in Metal Laser Sintering, International Solid Freeform Fabrication Symposium (2014) 1205–1212.

[22] J. Kruth, J. Deckers, E. Yasa, R. Wauthle, Assessing and comparing influencing factors of residual stresses in selective laser melting using a novel analysis method, Proceedings of the Institution of Mechanical Engineers, Part B: Journal of Engineering Manufacture 226 (6) (2012) 980–991.

[23] J. Kruth, L. Froyen, J. Van Vaerenbergh, P. Mercelis, M. Rombouts, B. Lauwers, Selective laser melting of iron-based powder, Journal of Materials Processing Technology 149 (1-3) (2004) 616–622.

[24] P. Mercelis, J.-P. Kruth, Residual stresses in selective laser sintering and selective laser melting, Rapid Prototyping Journal 12 (5) (2006) 254–265.

[25] S. Mohanty, C. C. Tutum, J. H. Hattel, Cellular scanning strategy for selective laser melting: Evolution of optimal grid-based scanning path & parametric approach to thermal homogeneity, in: Proc. of SPIE Vol, Vol. 8608, 2013, pp. 86080M–1.

[26] S. Mohanty, J. Hattel, Cellular scanning strategy for selective laser melting: capturing thermal trends with a low-fidelity, pseudo-analytical model, Mathematical Problems in Engineering 2014.

[27] S. Mohanty, J. H. Hattel, Cellular scanning strategy for selective laser melting: Generating reliable, optimized scanning paths and processing parameters 9353 (2015) 93530U.

[28] S. Mohanty, J. H. Hattel, Reducing residual stresses and deformations

in selective laser melting through multilevel multiscale optimization of cellular scanning strategy, in: Proc. of SPIE Vol, Vol. 9738, 2016, pp. 97380Z–1.

[29] P. OHara, C. Duarte, T. Eason, Generalized finite element analysis of three-dimensional heat transfer problems exhibiting sharp thermal gradients, Computer Methods in Applied Mechanics and Engineering 198 (2126) (2009) 1857 – 1871, advances in Simulation-Based Engineering Sciences Honoring J. Tinsley Oden.

[30] A. Fathi, E. Toyserkani, A. Khajepour, M. Durali, Prediction of melt pool depth and dilution in laser powder deposition, Journal of Physics D: Applied Physics 39 (12) (2006) 2613.

[31] A. V. Gusarov, T. Laoui, L. Froyen, Titov, V. I, Contact thermal conductivity of a powder bed in selective laser sintering, International Journal of Heat and Mass Transfer 46 (6) (2003) 1103–1109.

[32] I. Roberts, C. Wang, R. Esterlein, M. Stanford, D. Mynors, A three-dimensional finite element analysis of the temperature field during laser melting of metal powders in additive layer manufacturing, International Journal of Machine Tools and Manufacture 49 (12-13) (2009) 916–923.

[33] A. Robert, T. Debroy, Geometry of laser spot welds from dimensionless numbers, Metallurgical and Materials Transactions B 32 (October) (2001) 941–947.

[34] K. Kempen, B. Vrancken, L. Thijs, S. Buls, J. Humbeeck, J.-P. Kruth, Lowering thermal gradients in selective laser melting by pre-heating the baseplate, Solid Freeform Fabrication Symposium Proceedings, 2013.

[35] Y. Sato, M. Tsukamoto, S. Masuno, Y. Yamashita, Y. Yamashita, K. Yamashita, D. Tanigawa, N. Abe, Investigation of the microstructure and surface morphology of a Ti6Al4V plate fabricated by vacuum selective laser melting, Applied Physics A 122 (439) (2016) 1–5.

[36] T. Childs, M. Berzins, Selective laser sintering of an amorphous polymer-simulations and experiments, Journal of Engineering Manufacture 213 (4) (1999) 333–349.

[37] A. Surez, M. J. Tobar, A. Yez, I. Prez, J. Sampedro, V. Amig, J. J. Candel, Modeling of phase transformations of Ti6Al4V during laser metal deposition, Physics Procedia 12 (2011) 666–673.

[38] C. Ayas, J. A. W. Van Dommelen, V. S. Deshpande, Climb-enabled discrete dislocation plasticity, Journal of the Mechanics and Physics of Solids 62 (1) (2014) 113–136.

[39] H. Carslaw, J. Jaeger, Conduction of Heat in Solids, Oxford Science Publications, 1959.

[40] S. M. Dance, B. M. Shield, An image-source method for modelling sound in arbitrary enclosed spaces, Transactions on the Built Environment 10 (1995) 197–204.

[41] Y. Yang, C. Ayas, Point, surface and volumetric heat sources in the thermal modelling of selective laser melting, in: AIP Conference Proceedings, Vol. 1896, AIP Publishing, 2017, p. 040006.

[42] W. W. Wits, R. Bruins, L. Terpstra, R. A. Huls, H. J. M. Geijselaers, Single scan vector prediction in selective laser melting, Additive Manufacturing 9 (2016) 1–6.

[43] L. Parry, I. A. Ashcroft, R. D. Wildman, Understanding the effect of laser scan strategy on residual stress in selective laser melting through thermo-mechanical simulation, Additive Manufacturing 12 (2016) 1–15.

[44] M. Boivineau, C. Cagran, D. Doytier, V. Eyraud, M. H. Nadal, B. Wilthan, G. Pottlacher, Thermophysical properties of solid and liquid Ti-6Al-4V (TA6V) alloy, International Journal of Thermophysics 27 (2) (2006) 507–529.

[45] C. H. Fu, Y. B. Guo, Three-Dimensional Temperature Gradient Mechanism in Selective Laser Melting of Ti-6Al-4V, Journal of Manufacturing Science and Engineering 136 (6) (2014) 061004.

[46] L. Papadakis, A. Loizou, A thermo-mechanical modeling reduction approach for calculating shape distortion in SLM manufacturing for aero engine components, in: International Conference on Advanced Research in Virtual and Rapid Prototyping, 2013, pp. 613–618.

[47] Y. Yang, C. Ayas, Computationally efficient thermal-mechanical modelling of selective laser melting, in: AIP Conference Proceedings, Vol. 1896, AIP Publishing, 2017, p. 040005.